

Quasi-3D static analysis of two-directional functionally graded circular plates

Chih-Ping Wu* and Lu-Ting Yu

Department of Civil Engineering, National Cheng Kung University, Taiwan, ROC

(Received January 25, 2018, Revised April 2, 2018, Accepted April 6, 2018)

Abstract. A weak-form formulation of finite annular prism methods (FAPM) based on Reissner's mixed variational theorem (RMVT), is developed for the quasi three-dimensional (3D) static analysis of two-directional functionally graded (FG) circular plates with various boundary conditions and under mechanical loads. The material properties of the circular plate are assumed to obey either a two-directional power-law distribution of the volume fractions of the constituents through the radial-thickness surface or an exponential function distribution varying doubly exponentially through it. These FAPM solutions of the loaded FG circular plates with both simply-supported and clamped edges are in excellent agreement with the solutions obtained using the 3D analytical approach and two-dimensional advanced plate theories available in the literature.

Keywords: circular plates; finite annular prism methods; functionally graded material; Reissner's mixed variational theorem; rule of mixtures; various boundary conditions

1. Introduction

It is well known that fiber-reinforced laminated composite (FRLC) structures have a sudden change in their material properties when they cross the interfaces between adjacent layers due to the fact that two dissimilar materials have bonded together. As a result, residual stresses always concentrate around these interfaces when the FRLC structures are subjected to external mechanical and thermal loads and cause the FRLC structures to be prone to delamination in these areas. Thus, in lieu of FRLC materials, a new class of materials, the so-called functionally graded materials (FGM), was introduced by a group of scientists in Sendai, Japan in 1984 (Koizumi 1997, Miyamoto *et al.* 1999), to form various beam-, plate-, and shell-like structures in advanced engineering in order to prevent the above-mentioned weakness that typically occurs in FRLC structures. The material properties of these FGM structures are designed to vary continuously and smoothly with the thickness coordinate according to the predefined distributions of the volume fractions of the constituents. Along with the increasing popularity of FGM structures, the related structural analyses have attracted considerable attention. Some review articles on the theoretical methodologies and numerical models of FGM beams, plates, and shells can be found in the literature (Carrera and Brischetto 2009, Liew *et al.* 2015, Wu and Liu 2016a). Among these, the review conducted in this work will focus on articles related to the structural analyses of FGM circular plates.

Some two-dimensional (2D) advanced and refined plate theories and the three-dimensional (3D) elasticity theory have been used for assorted analyses of one-directional

functionally graded (FG) circular plates with simply-supported or clamped boundary conditions that are subjected to uniformly distributed loads. Among these, the material properties of the FG circular plate considered in most of the articles were assumed to vary through the thickness direction and remain unchanged over the circumferential-radial surface, which are the so-called one-directional FG circular plates. The articles examining the structural behavior of two-directional FG circular plates are rare in the public literature as compared with those for one-directional FG and laminated composite circular plates.

Based on the first-order shear deformation theory (FSDT), Reddy *et al.* (1999) investigated the axisymmetric bending and stretching behavior of FG circular and annular plates. A two-phase (ceramic-metal) composite material was used to form the plate, the material properties of which were assumed to obey the power-law distribution through the thickness direction according to the volume fractions of the constituents, and the effective material properties were estimated using the rules of mixtures. The FSDT was also extended by Boudarba *et al.* (2016) to the thermal buckling problem of FG sandwich plates. The above-mentioned issue was also studied by Saidi *et al.* (2009) and Sahraee and Saidi (2009) using an unconstrained third-order shear deformation theory (TSDT) and a fourth-order shear deformation theory (FOSDT), respectively. Numerical results for displacement and stress components induced in the one-directional FG circular plates were presented for different values of material-property gradient indices. Tornabene and Viola (2009a, b) and Tornabene (2009) extended the FSDT to the free vibration analysis of one-directional power-law-type FG parabolic and circular panels, as well as various shells of revolution, such as conical shells, cylindrical shells and annular plates. Based on a new simple three-unknown shear deformation theory, Hachemi *et al.* (2017) and Houari *et al.* (2016) examined

*Corresponding author, Ph.D., Professor,
E-mail: cpwu@mail.ncku.edu.tw

the bending behavior of one-directional FG plates with and without resting on an elastic medium, respectively. Sobhy (2016) proposed a four-variable shear deformation theory to examine the vibration and buckling behavior of power-law-type FG sandwich plates in hygrothermal environment. Abdelaziz *et al.* (2017) developed an efficient hyperbolic shear deformation theory for a variety of mechanical analyses of sandwich FG plates, such as bending, buckling, and free vibration. Elmoossouess *et al.* (2017) developed a new higher-order shear deformation theory (HSDT) for the thermal buckling analysis of FG sandwich plates, in which the total number of primary variables of the theory is taken to be four only, which is even less than that of FSDT and conventional HSDT. Based on various shear deformation theories, Sobhy (2013) dealt with the vibration and buckling behavior of exponent function-type FG sandwich plates resting on elastic foundations. Bouchafa *et al.* (2015) presented the results with regard to the thermal stress and deflection components induced in an FG sandwich plate subjected to thermo-mechanical loads using a new refined hyperbolic shear deformation theory, in which a parametric study regarding effects of the shear deformation, aspect ratios, and material-property gradient index on the coupled thermo-elastic behavior of the plate were carried out. Based on a sinusoidal shear deformation theory, Sobhy (2015) investigated the thermoelastic response of power-law-type FG plates with temperature-dependent properties resting on variable elastic foundations. Some weak formulations on the basis of differential and integral quadrature methods have also been developed for the free vibration analysis of composite plates and shells (Tornabene *et al.* 2017a, 2017b).

Within the framework of 3D elasticity theory, Wang *et al.* (2010) studied the axisymmetric bending behavior of transversely isotropic and FG circular plates using the direct displacement method (DDM). The material properties were assumed to obey the exponential function distribution through the thickness direction, the applied external load was expanded as a series of Fourier-Bessel functions, and the superposition principle was used to obtain the final results by summarizing the results of each individual external force. The DDM was extended to the 3D coupled thermo-elastic analysis of FG circular plates under axisymmetric thermo-mechanical loads by Li *et al.* (2012) and Jabbari *et al.* (2014), and the analysis of axisymmetric buckling and vibration of FG circular and annular plates by Xu *et al.* (2005) and Wang *et al.* (2009), respectively. Pendhari *et al.* (2012) presented mixed semi-analytical and analytical solutions for the static problems of simply-supported, one-directional FG rectangular plates. Based on the 3D elasticity theory, Tahounh (2014) studied the free vibration behavior of bidirectional FG annular plates resting on the Pasternak-type foundation using the differential quadrature method.

In order to not only capture the 3D behavior of FGM plates and shells, such as the thickness effect, but also to overcome the restrictions of 3D analytical methods, such as the complicated solution process and difficulty associated with use for one- and multi-directional FG circular plates, on the basis of Reissner's mixed variational theorem

(RMVT), Wu and Li (2013a, b) developed the finite rectangular prism method (FRPM) and finite cylindrical prism method (FCPM) for the quasi-3D analysis of one-directional FG rectangular plates and cylinders with various boundary conditions, respectively. Implementation of the RMVT-based FRPM and FCPM showed that their solutions are accurate and converge rapidly. In the current article, the RMVT is extended to develop the finite annular prism method (FAPM) for the quasi-3D static analysis of two-directional FG circular plates with both simply-supported and clamped boundary conditions. The material properties of the FGM circular plate are assumed to obey either a two-directional power-law distribution of the volume fractions of the constituents through the radial-thickness surface or an exponential function distribution varying doubly exponentially through the radial-thickness surface. The number of nodes on the nodal surface of each prism can be set at four for the linear FAPM, and at eight and 12 for the quadratic and cubic FAPM of the serendipity-family. A parametric study with regard to some key effects on the quasi-3D static behavior of two-directional FG circular plates with various boundary conditions is carried out, such as the material-property gradient indices, aspect ratios, and different boundary conditions.

2. RMVT-based finite annular prism methods

The authors consider an N_l -layered two-directional FG circular plate subjected to a trigonometrically (or uniformly) distributed load on the top surface of the circular plate, as shown in Fig. 1, in which N_l is the total number of the layers constituting the circular plate. The thickness and mid-surface radius of the circular plate are defined as h and R , respectively. The thickness of each individual layer is

$h_m (m = 1, 2, \dots, N_l)$, such that $h = \sum_{m=1}^{N_l} h_m$. The boundary

conditions of the circular plate are considered as either the clamped or simply-supported boundary conditions. The cylindrical global coordinate system (i.e., r , θ and z coordinates) is located on the mid-surface of the circular plate. The typical four-node linear, eight-node quadratic, and 12-node cubic annular prisms of the serendipity-family in the natural coordinate system are shown in Fig. 2, in which (ξ, η) denotes the natural coordinates, which are located at the center of the nodal surface of a typical annular prism (i.e., the radial-thickness surface). The mapping relations between the global and natural coordinates of each point in the prism domain are expressed

as $r^{(e)} = \sum_{i=1}^{n_s} r_i^{(e)} \psi_i^{(e)}(\xi, \eta)$ and $z^{(e)} = \sum_{i=1}^{n_s} z_i^{(e)} \psi_i^{(e)}(\xi, \eta)$,

in which n_s denotes the degree of approximation used to describe the coordinate transformation for the annular prism, and $\psi_i^{(e)}(\xi, \eta)$, $i = 1 - n_s$, denote the shape (or interpolation) functions of the annular prism. Since the isoparametric annular prisms are used in the implementation of these FAPM, i.e., the degree of approximation used to describe the coordinate transformation is equal to that used

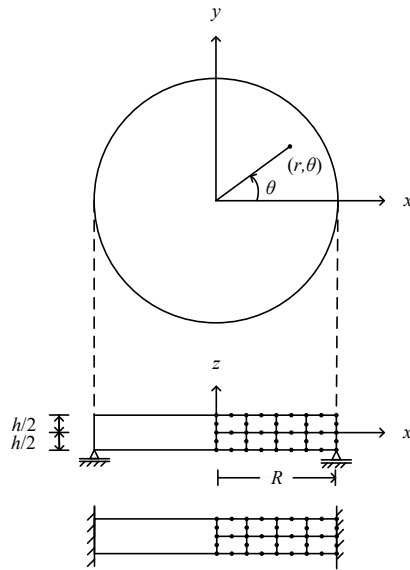


Fig. 1 The configuration, cylindrical coordinate system and boundary conditions of a circular plate with a 4x2 mesh of the Q8 FAPM

to represent each primary field variable, such that the values of n_s are taken to be four, eight, and 12 for the linear, quadratic, and cubic FAPM, respectively.

2.1 Kinematic and kinetic assumptions

The displacement and transverse stress components of a typical annular prism of the m th-layer are given by (Wu and Li 2013b)

$$[u_r^{(e)}(r, \theta, z)]^{(m)} = \sum_{i=1}^{n_d} [\psi^{(e)}(r, z)]_i [u^{(e)}(\theta)]_i^{(m)} \quad (1)$$

$$[u_\theta^{(e)}(r, \theta, z)]^{(m)} = \sum_{i=1}^{n_d} [\psi^{(e)}(r, z)]_i [v^{(e)}(\theta)]_i^{(m)} \quad (2)$$

$$[u_z^{(e)}(r, \theta, z)]^{(m)} = \sum_{i=1}^{n_d} [\psi^{(e)}(r, z)]_i [w^{(e)}(\theta)]_i^{(m)} \quad (3)$$

$$[\tau_{rz}^{(e)}(r, \theta, z)]^{(m)} = \sum_{i=1}^{n_d} [\psi^{(e)}(r, z)]_i [\tau_{13}^{(e)}(\theta)]_i^{(m)} \quad (4)$$

$$[\tau_{\theta z}^{(e)}(r, \theta, z)]^{(m)} = \sum_{i=1}^{n_d} [\psi^{(e)}(r, z)]_i [\tau_{23}^{(e)}(\theta)]_i^{(m)} \quad (5)$$

$$[\sigma_z^{(e)}(r, \theta, z)]^{(m)} = \sum_{i=1}^{n_d} [\psi^{(e)}(r, z)]_i [\sigma_3^{(e)}(\theta)]_i^{(m)} \quad (6)$$

where $(u^{(e)})_i^{(m)}, (v^{(e)})_i^{(m)}, (w^{(e)})_i^{(m)}, (\tau_{13}^{(e)})_i^{(m)}, (\tau_{23}^{(e)})_i^{(m)}, (\sigma_3^{(e)})_i^{(m)}$ with $(i=1, 2, \dots, n_d)$ are the nodal displacement and transverse stress components of a typical annular prism of the m th-layer of the circular plate; n_d denotes the total

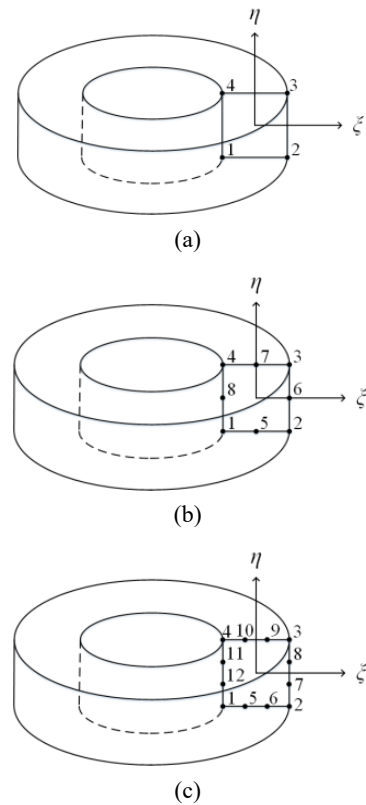


Fig. 2 The configuration of a typical finite annular prism: (1) L4; (b) Q8; and (c) C12

number of nodes of a typical annular prism, such that the values of n_d are four, eight and 12 for the linear, quadratic and cubic annular prisms, respectively. The symbols, L4, Q8, and C12, will be used later in this work to represent four-node linear, eight-node quadratic, and 12-node cubic annular prisms. $(\psi^{(e)})_i^{(m)} (i=1, \dots, n_d)$ are the corresponding shape (or interpolation) functions used to interpolate the primary field variables over the prism domain.

The linear constitutive equations of the m th-layer, which are valid for the orthotropic materials, are given by

$$\begin{Bmatrix} \sigma_r^{(m)} \\ \sigma_\theta^{(m)} \\ \sigma_z^{(m)} \\ \tau_{\theta z}^{(m)} \\ \tau_{rz}^{(m)} \\ \tau_{r\theta}^{(m)} \end{Bmatrix} = \begin{bmatrix} c_{11}^{(m)} & c_{12}^{(m)} & c_{13}^{(m)} & 0 & 0 & 0 \\ c_{12}^{(m)} & c_{22}^{(m)} & c_{23}^{(m)} & 0 & 0 & 0 \\ c_{13}^{(m)} & c_{23}^{(m)} & c_{33}^{(m)} & 0 & 0 & 0 \\ 0 & 0 & 0 & c_{44}^{(m)} & 0 & 0 \\ 0 & 0 & 0 & 0 & c_{55}^{(m)} & 0 \\ 0 & 0 & 0 & 0 & 0 & c_{66}^{(m)} \end{bmatrix} \begin{Bmatrix} \epsilon_r^{(m)} \\ \epsilon_\theta^{(m)} \\ \epsilon_z^{(m)} \\ \gamma_{\theta z}^{(m)} \\ \gamma_{rz}^{(m)} \\ \gamma_{r\theta}^{(m)} \end{Bmatrix} \quad (7)$$

where $\sigma_r^{(m)}, \sigma_\theta^{(m)}, \dots$ and $\tau_{r\theta}^{(m)}$ are the stress components; $\epsilon_r^{(m)}, \epsilon_\theta^{(m)}, \dots$ and $\gamma_{r\theta}^{(m)}$ are the strain components; $c_{ij}^{(m)}$ are the elastic coefficients, which are considered to be independent of the circumferential coordinate in the analysis, while they are variable over the radial-thickness surface of the annular prism (i.e., $c_{ij}^{(m)}(r, z)$).

The strain-displacement relations for a typical annular prism of the m th-layer, based on the assumed displacement components in Eqs. (1)-(3), are given by

$$[\varepsilon_r^{(e)}(r, \theta, z)]^{(m)} = \sum_{i=1}^{n_d} (D_r \psi_i^{(e)})(u_i^{(e)})^{(m)} \quad (8)$$

$$[\varepsilon_\theta^{(e)}(r, \theta, z)]^{(m)} = (1/r) \sum_{i=1}^{n_d} (\psi_i^{(e)})(v_i^{(e)}, \theta)^{(m)} \\ + (1/r) \sum_{i=1}^{n_d} (\psi_i^{(e)})(u_i^{(e)})^{(m)} \quad (9)$$

$$[\varepsilon_z^{(e)}(r, \theta, z)]^{(m)} = \sum_{i=1}^{n_d} (D_z \psi_i^{(e)})(w_i^{(e)})^{(m)} \quad (10)$$

$$[\gamma_{rz}^{(e)}(r, \theta, z)]^{(m)} = \sum_{i=1}^{n_d} (D_z \psi_i^{(e)})(u_i^{(e)})^{(m)} \\ + \sum_{i=1}^{n_d} (D_r \psi_i^{(e)})(w_i^{(e)})^{(m)} \quad (11)$$

$$[\gamma_{\theta z}^{(e)}(r, \theta, z)]^{(m)} = \sum_{i=1}^{n_d} (D_z \psi_i^{(e)})(v_i^{(e)})^{(m)} \\ + (1/r) \sum_{i=1}^{n_d} (\psi_i^{(e)})(w_i^{(e)}, \theta)^{(m)} \quad (12)$$

$$[\gamma_{r\theta}^{(e)}(r, \theta, z)]^{(m)} \\ = (1/r) \sum_{i=1}^{n_d} (\psi_i^{(e)})(u_i^{(e)}, \theta)^{(m)} \\ + \sum_{i=1}^{n_d} (D_r \psi_i^{(e)})(v_i^{(e)})^{(m)} - (1/r) \sum_{i=1}^{n_d} (\psi_i^{(e)})(v_i^{(e)})^{(m)} \quad (13)$$

where the commas denote partial differentiation with respect to the suffix variables, and $D_r \psi_i^{(e)} = \partial \psi_i^{(e)} / \partial r$, $D_z \psi_i^{(e)} = \partial \psi_i^{(e)} / \partial z$.

2.2 The Reissner mixed variational theorem

The Reissner mixed variational theorem is used to derive the static equilibrium equations of the FG circular plate under mechanical loads, and the corresponding energy functional (Π_R) of the loaded plate is written in the form of

$$\Pi_R = \int_{-h/2}^{h/2} \int_0^{2\pi} \int_0^R [\sigma_r \varepsilon_r + \sigma_\theta \varepsilon_\theta + \sigma_z \varepsilon_z + \tau_{rz} \gamma_{rz} \\ + \tau_{\theta z} \gamma_{\theta z} + \tau_{r\theta} \gamma_{r\theta} - B(\sigma_{ij})] r dr d\theta dz \\ - \iint_{\Omega^+} [\bar{q}_k^+(r, \theta) u_k^+(r, \theta, h/2)] r dr d\theta \\ - \iint_{\Omega^-} [\bar{q}_k^-(r, \theta) u_k^-(r, \theta, -h/2)] r dr d\theta \\ - \int_{-h/2}^{h/2} \int_{\Gamma_\sigma} (\bar{t}_k u_k) d\Gamma dz - \int_{-h/2}^{h/2} \int_{\Gamma_u} [(u_k - \bar{u}_k) t_k] d\Gamma dz \quad (14)$$

where Ω^+ and Ω^- denote the top and bottom surfaces of the circular plate (i.e., $z = h/2$ and $z = -h/2$), respectively, in which the transverse loads \bar{q}_k^+ and \bar{q}_k^- ($k = r, \theta$ and z)

are applied, the upward ones of which are defined as positive; Γ_σ and Γ_u denote the portions of the edge boundary, in which the surface traction and displacement components (i.e., \bar{t}_k and \bar{u}_k ($k = r, \theta$ and z)) are prescribed, respectively. $B(\sigma_{ij})$ is the complementary energy density function.

In the current formulation, the RMVT is used, such that the displacement and transverse stress components are taken as the primary variables subject to variation. Using the kinematic and kinetic assumptions, given in Eqs. (1)-(3) and (4)-(6), respectively, the authors perform the first-order variation of the Reissner energy functional as zero, as follows

$$\delta \Pi_R = \sum_{m=1}^{N_l} \sum_{e=1}^{N_e} \left\{ \int_0^{2\pi} \int_{A_e} \left[(\delta \varepsilon_p^{(e)})^T \sigma_p^{(e)} + (\delta \varepsilon_s^{(e)})^T \sigma_s^{(e)} \right. \right. \\ \left. \left. + \delta \varepsilon_z^{(e)} \sigma_z^{(e)} + (\delta \sigma_s^{(e)})^T (\varepsilon_s^{(e)} - \mathbf{S}^{(e)} \sigma_s^{(e)}) \right. \right. \\ \left. \left. + \delta \sigma_z^{(e)} \left[\varepsilon_z^{(e)} - (c_{33}^{(e)})^{-1} \sigma_z^{(e)} + (\mathbf{Q}_z^{(e)})^T \varepsilon_p^{(e)} \right] \right\} r dA_e d\theta \\ - \sum_{e=1}^{N_e} \int_{\theta=0}^{\theta=2\pi} \int_{r_e}^{r_{e+1}} \left\{ \bar{q}_k^+(r, \theta) (\psi_k^{(e)}(r, z = h/2))_j^{(m=N_l)} \right. \\ \left. [\delta u_k^{(e)}(z = h/2)]_j^{(m=N_l)} \right\} r dr d\theta \\ - \sum_{e=1}^{N_e} \int_{\theta=0}^{\theta=2\pi} \int_{r_e}^{r_{e+1}} \left\{ \bar{q}_k^-(r, \theta) (\psi_k^{(e)}(r, z = -h/2))_j^{(m=1)} \right. \\ \left. [\delta u_k^{(e)}(z = -h/2)]_j^{(m=1)} \right\} r dr d\theta = 0 \quad (15)$$

where N_e denotes the number of annular prisms in each individual layer; A_e is defined as the cross-sectional area of a typical annular prism, such that $dA_e = dr \times dz$; the superscript of T denotes the transposition of the matrices or vectors; and

$$\varepsilon_p^{(e)} = [\varepsilon_r^{(e)} \ \varepsilon_\theta^{(e)} \ \gamma_{r\theta}^{(e)}]^T = \mathbf{B}_1^{(e)} \mathbf{u}^{(e)}, \\ \sigma_p^{(e)} = [\sigma_r^{(e)} \ \sigma_\theta^{(e)} \ \tau_{r\theta}^{(e)}]^T = \mathbf{Q}_p^{(e)} \mathbf{B}_1^{(e)} \mathbf{u}^{(e)} + \mathbf{Q}_z^{(e)} \mathbf{B}_2^{(e)} \sigma^{(e)}, \\ \varepsilon_s^{(e)} = [\gamma_{rz}^{(e)} \ \gamma_{\theta z}^{(e)}]^T = \mathbf{B}_3^{(e)} \mathbf{u}^{(e)} + \mathbf{B}_4^{(e)} \mathbf{w}^{(e)}, \\ \sigma_s^{(e)} = [\tau_{rz}^{(e)} \ \tau_{\theta z}^{(e)}]^T = \mathbf{B}_5^{(e)} \tau^{(e)}, \quad \varepsilon_z^{(e)} = \mathbf{B}_6^{(e)} \mathbf{w}^{(e)}, \\ \sigma_z^{(e)} = \mathbf{B}_2^{(e)} \sigma^{(e)}, \quad \mathbf{u}^{(e)} = \begin{bmatrix} u_i^{(e)} \\ v_i^{(e)} \end{bmatrix}, \quad \mathbf{w}^{(e)} = [w_i^{(e)}] \\ \tau^{(e)} = \begin{bmatrix} \tau_{13}^{(e)} \\ \tau_{23}^{(e)} \end{bmatrix}_i, \quad \sigma^{(e)} = [(\sigma_3^{(e)})_i], \quad \mathbf{S}^{(e)} = \begin{bmatrix} (1/c_{55}^{(e)}) & 0 \\ 0 & (1/c_{44}^{(e)}) \end{bmatrix}, \\ \mathbf{Q}_p^{(e)} = \begin{bmatrix} Q_{11}^{(e)} & Q_{12}^{(e)} & 0 \\ Q_{12}^{(e)} & Q_{22}^{(e)} & 0 \\ 0 & 0 & Q_{66}^{(e)} \end{bmatrix}, \quad \mathbf{Q}_z^{(e)} = \begin{bmatrix} Q_{13}^{(e)} \\ Q_{23}^{(e)} \\ 0 \end{bmatrix}, \\ \mathbf{B}_1^{(e)} = \begin{bmatrix} (D_r \psi_i^{(e)}) & 0 \\ (1/r) \psi_i^{(e)} & (1/r) \psi_i^{(e)} \partial_\theta \\ (1/r) \psi_i^{(e)} \partial_\theta & (D_r \psi_i^{(e)}) - (1/r) \psi_i^{(e)} \end{bmatrix}, \\ \mathbf{B}_2^{(e)} = [(\psi_i^{(e)})], \quad \mathbf{B}_3^{(e)} = \begin{bmatrix} (D_z \psi_i^{(e)}) & 0 \\ 0 & (D_z \psi_i^{(e)}) \end{bmatrix},$$

$$\mathbf{B}_4^{(e)} = \begin{bmatrix} (D_r \psi_i^{(e)}) \\ (1/r)(\psi_i^{(e)}) \partial_{\theta} \end{bmatrix}, \quad \mathbf{B}_5^{(e)} = \begin{bmatrix} (\psi_i^{(e)}) & 0 \\ 0 & (\psi_i^{(e)}) \end{bmatrix},$$

$$\mathbf{B}_6^{(e)} = \left[(D_z \psi_i^{(e)}) \right]$$

in which $i = 1, 2, \dots, n_d$;

$$Q_{kl}^{(e)} = c_{kl}^{(e)} - (c_{k3}^{(e)} c_{l3}^{(e)} / c_{33}^{(e)}) \quad (k, l = 1 \text{ and } 2),$$

$$Q_{k3}^{(e)} = c_{k3}^{(e)} / c_{33}^{(e)} \quad (k = 1 \text{ and } 2), \quad Q_{66}^{(e)} = c_{66}^{(e)}.$$

2.3 Euler-Lagrange equations

The static behavior of a multilayered FG circular plate with either simply-supported or clamped boundary edges under mechanical loads is studied in the following illustrative examples, in which the material properties are considered as either a two-directional power-law distribution or an exponential function one over the radial-thickness surface, while they are independent of the circumferential direction. The applied loading conditions on the top and bottom surfaces of the circular plate are prescribed as

$$\begin{bmatrix} \tau_{rz}^{(Nl)}(r, \theta, h/2) & \tau_{\theta z}^{(Nl)}(r, \theta, h/2) & \sigma_z^{(Nl)}(r, \theta, h/2) \end{bmatrix} = \begin{bmatrix} 0 & 0 & \bar{q}_z^+(x, \theta) \end{bmatrix} \text{ on } z = h/2 \quad (16a)$$

$$\begin{bmatrix} \tau_{rz}^{(l)}(r, \theta, -h/2) & \tau_{\theta z}^{(l)}(r, \theta, -h/2) & \sigma_z^{(l)}(r, \theta, -h/2) \end{bmatrix} = \begin{bmatrix} 0 & 0 & 0 \end{bmatrix} \text{ on } z = -h/2 \quad (16b)$$

where \bar{q}_z^+ are expressed as the single Fourier series and given as $\bar{q}_z^+ = \sum_{\hat{n}=0}^{\infty} \bar{q}_{\hat{n}} \cos(\hat{n}\theta)$ in which \hat{n} is either a positive integer or zero.

The boundary edge at $r = R$ is considered to be either the clamped or simply-supported edge, the corresponding boundary conditions of which are given as follows:

For clamped (C) supports

$$u_r^{(e)} = u_{\theta}^{(e)} = u_z^{(e)} = 0 \quad (17a)$$

For simple (S) supports

$$u_{\theta}^{(e)} = u_z^{(e)} = \sigma_r^{(e)} = 0 \quad (17b)$$

The continuity conditions at the center of the circular plate ($r = 0$) are given as

$$u_r^{(e)} = u_{\theta}^{(e)} = \tau_{rz}^{(e)} = 0 \quad (18)$$

Using the separation of variables, the authors expand the primary field variables of each individual annular prism, which are given in Eqs. (1)-(6), as the single Fourier series in the circumferential coordinate, and they are rewritten as

$$(u_r^{(e)})^{(m)} = \sum_{\hat{n}=0}^{\infty} \sum_{i=1}^{n_d} (\psi_i^{(e)}) (u_{\hat{n}}^{(e)})^{(m)} \cos \hat{n}\theta \quad (19)$$

$$(u_{\theta}^{(e)})^{(m)} = \sum_{\hat{n}=0}^{\infty} \sum_{i=1}^{n_d} (\psi_i^{(e)}) (v_{\hat{n}}^{(e)})^{(m)} \sin \hat{n}\theta \quad (20)$$

$$(u_z^{(e)})^{(m)} = \sum_{\hat{n}=0}^{\infty} \sum_{i=1}^{n_d} (\psi_i^{(e)}) (w_{\hat{n}}^{(e)})^{(m)} \cos \hat{n}\theta \quad (21)$$

$$(\tau_{rz}^{(e)})^{(m)} = \sum_{\hat{n}=0}^{\infty} \sum_{i=1}^{n_d} (\psi_i^{(e)}) (\tau_{13\hat{n}}^{(e)})^{(m)} \cos \hat{n}\theta \quad (22)$$

$$(\tau_{\theta z}^{(e)})^{(m)} = \sum_{\hat{n}=0}^{\infty} \sum_{i=1}^{n_d} (\psi_i^{(e)}) (\tau_{23\hat{n}}^{(e)})^{(m)} \sin \hat{n}\theta \quad (23)$$

$$(\sigma_z^{(e)})^{(m)} = \sum_{\hat{n}=0}^{\infty} \sum_{i=1}^{n_d} (\psi_i^{(e)}) (\sigma_{3\hat{n}}^{(e)})^{(m)} \cos \hat{n}\theta \quad (24)$$

Introducing the kinetic and kinematic models of the FAPMs (Eqs. (19)-(24)) and the boundary conditions on the top and bottom surfaces (Eqs. (16a) and (16b)) in Eq. (15) and imposing the stationary principle of the Reissner energy functional (i.e., $\delta \Pi_R = 0$), we thus obtain the Euler-Lagrange equations of the FG circular plate as follows

$$\sum_{m=1}^{N_l} \sum_{e=1}^{N_e} \begin{bmatrix} \mathbf{K}_{I \ I}^{(e)} & \mathbf{0} & \mathbf{K}_{I \ III}^{(e)} & \mathbf{K}_{I \ IV}^{(e)} \\ \mathbf{0} & \mathbf{0} & \mathbf{K}_{II \ III}^{(e)} & \mathbf{K}_{II \ IV}^{(e)} \\ \mathbf{K}_{III \ I}^{(e)} & \mathbf{K}_{III \ II}^{(e)} & \mathbf{K}_{III \ III}^{(e)} & \mathbf{0} \\ \mathbf{K}_{IV \ I}^{(e)} & \mathbf{K}_{IV \ II}^{(e)} & \mathbf{0} & \mathbf{K}_{IV \ IV}^{(e)} \end{bmatrix}^{(m)} \begin{bmatrix} \tilde{\mathbf{u}}^{(e)} \\ \tilde{\mathbf{w}}^{(e)} \\ \tilde{\boldsymbol{\tau}}^{(e)} \\ \tilde{\boldsymbol{\sigma}}^{(e)} \end{bmatrix}^{(m)} = \delta_{mN_l} \sum_{e=1}^{N_e} \begin{bmatrix} \mathbf{0} \\ \mathbf{P}^{(e)} \\ \mathbf{0} \\ \mathbf{0} \end{bmatrix}^{(m)} \quad (25)$$

where

$$(\mathbf{K}_{i \ j}^{(e)})^{(m)} = \left[(\mathbf{K}_{j \ i}^{(e)})^{(m)} \right]^T \quad ((i, j = \text{I, II, III, IV});$$

$$(\mathbf{K}_{I \ I}^{(e)})^{(m)} = \iint_{A_e} (\tilde{\mathbf{B}}_1^{(e)})^T \mathbf{Q}_p^{(e)} \tilde{\mathbf{B}}_1^{(e)} r dA_e,$$

$$(\mathbf{K}_{I \ III}^{(e)})^{(m)} = \iint_{A_e} (\mathbf{B}_3^{(e)})^T \mathbf{B}_5^{(e)} r dA_e,$$

$$(\mathbf{K}_{I \ IV}^{(e)})^{(m)} = \iint_{A_e} (\tilde{\mathbf{B}}_1^{(e)})^T \mathbf{Q}_z^{(e)} \mathbf{B}_2^{(e)} r dA_e,$$

$$(\mathbf{K}_{II \ III}^{(e)})^{(m)} = \iint_{A_e} (\tilde{\mathbf{B}}_4^{(e)})^T \mathbf{B}_5^{(e)} r dA_e,$$

$$(\mathbf{K}_{II \ IV}^{(e)})^{(m)} = \iint_{A_e} (\mathbf{B}_6^{(e)})^T \mathbf{B}_2^{(e)} r dA_e,$$

$$(\mathbf{K}_{III \ III}^{(e)})^{(m)} = -\iint_{A_e} (\mathbf{B}_5^{(e)})^T \mathbf{S}^{(e)} \mathbf{B}_5^{(e)} r dA_e,$$

$$(\mathbf{K}_{IV \ IV}^{(e)})^{(m)} = -\iint_{A_e} (1/c_{33}^{(e)}) (\mathbf{B}_2^{(e)})^T \mathbf{B}_2^{(e)} r dA_e,$$

$$\tilde{\mathbf{u}}^{(m)} = \begin{bmatrix} (u_{\hat{n}}^{(e)})^{(m)} \\ (v_{\hat{n}}^{(e)})^{(m)} \end{bmatrix}, \quad \tilde{\mathbf{w}}^{(m)} = \left[(w_{\hat{n}}^{(e)})^{(m)} \right], \quad \tilde{\boldsymbol{\tau}}^{(m)} = \begin{bmatrix} (\tau_{13\hat{n}}^{(e)})^{(m)} \\ (\tau_{23\hat{n}}^{(e)})^{(m)} \end{bmatrix},$$

$$\tilde{\boldsymbol{\sigma}}^{(m)} = \left[(\sigma_{3\hat{n}}^{(e)})^{(m)} \right] \text{ in which } i = 1 - n_d;$$

$$(\mathbf{P}^{(e)})^{(N_l)} = \int_{r_e}^{r_e+1} (\bar{q}_{\hat{n}}) \psi_i^{(e)}(r, z = h/2) r dr;$$

δ_{mN_i} is the Kronecker delta symbol, in which $\delta_{mN_i} = 0$ when $m \neq N_i$, and $\delta_{N_i N_i} = 1$.

By imposing the continuity conditions of each node's nodal primary variables, i.e., the nodal displacement and transverse stress components, at the nodal lines between adjacent prisms, the local stiffness matrix and forcing vector of each prism in Eq. (25) can be assembled as their corresponding global stiffness matrix and forcing vector of the FG circular plate. The nodal primary variables at each node of the prism can then be determined. Subsequently, the variables of the in-plane stresses at the nodes can be obtained using the primary variables, which were determined, and are given by

$$\left(\sigma_r^{(e)}, \sigma_\theta^{(e)} \right)^{(m)} = \sum_{\hat{n}=0}^{\infty} \left(\sigma_{1\hat{n}}^{(e)}, \sigma_{2\hat{n}}^{(e)} \right)^{(m)} \cos \hat{n} \theta \quad (26)$$

$$\left(\tau_{r\theta}^{(e)} \right)^{(m)} = \sum_{\hat{n}=0}^{\infty} \left(\tau_{12\hat{n}}^{(e)} \right)^{(m)} \sin \hat{n} \theta \quad (27)$$

where

$$\left[\left(\sigma_{1\hat{n}}^{(e)} \right)^{(m)} \left(\sigma_{2\hat{n}}^{(e)} \right)^{(m)} \left(\tau_{12\hat{n}}^{(e)} \right)^{(m)} \right]^T = \mathbf{Q}_p^{(e)} \tilde{\mathbf{B}}_1^{(e)} \tilde{\mathbf{u}}^{(e)} + \mathbf{Q}_z^{(e)} \mathbf{B}_2^{(e)} \tilde{\sigma}^{(e)}$$

Using the above-mentioned weak-form formulation of the RMVT-based FAPM, the authors investigate the quasi-3D static behavior of two-directional FG circular plates with both simply-supported and clamped boundary conditions under mechanical loads in the following illustrative examples, and the performance of the current RMVT-based L4, Q8, and C12 FAPM is also examined.

3. Illustration examples

3.1 One- and two-directional power-law-type FG circular plates

In this section, the authors examine the static behavior of a one-directional power-law-type FG circular plate with simply-supported and clamped boundary conditions under a uniformly distributed load, i.e., $\bar{q}_z^+ = q_0$ and $\bar{q}_z^- = 0$, such that the half wave number \hat{n} in the current formulation is identical to zero. The problem was previously investigated by Reddy *et al.* (1999), Saidi *et al.* (2009) and Sahraee and Saidi (2009) using 2D advanced and refined plate theories, such as FSDT, TSDT, and FOSDT, respectively, and was also investigated by Wang *et al.* (2010) and Wu and Liu (2016b) using the state space analytical method and the state space differential reproducing kernel (SSDRK) method, respectively, and the corresponding solutions are thus used to validate the solutions obtained using the current L4, Q8 and C12 FAPM.

The circular plate considered is composed of ceramic and metal materials according to a one-directional power-law distribution of volume fractions of the constituents through the thickness coordinate. The effective material

properties are estimated using the rule of mixtures, in which the Poisson's ratio ν remains a constant (i.e., $\nu = 0.288$), while Young's modulus is in the form of

$$E(z) = E_c + (E_m - E_c) \Gamma_m(z) \quad (28)$$

where $\Gamma_m(z)$ denotes the volume fraction of the metal material, and $\Gamma_m(z) = [(1/2) - (z/h)]^{\kappa_{pz}}$. E_m and E_c represent the Young's moduli of the metal and ceramic materials, respectively, and the ratio of E_m/E_c is taken to be 0.396. The superscript, κ_{pz} , denotes the material-property gradient index in the thickness direction. When $\kappa_{pz} = 0$ and $\kappa_{pz} = \infty$, the FG circular plate will reduce to the homogeneous metal and ceramic plates, respectively, while in the cases of other values of κ_{pz} , the top and bottom surfaces of the FGM plate are ceramic- and metal-rich, respectively.

Tables 1 and 2 show the convergence studies for the current L4, Q8, and C12 FAPM solutions of the displacement components at the center of the FG circular plate with clamped and simply-supported boundary conditions, respectively, under a uniform load. The dimensionless displacement is defined as $\bar{u}_z = [(64 D_c)/(q_0 R^4)] u_z(0, \theta, 0)$, in which $D_c = (E_c h^3)/[12(1-\nu^2)]$. When using the current FAPM, the uniform meshes on the nodal surface (i.e., the radial-thickness surface) are taken to be $(n_r \times n_z) = (8 \times 2)$, (8×4) , (16×4) and (32×8) . The material-property gradient indices κ_{pz} of the FG circular plate are considered to be $\kappa_{pz} = 2, 5$, and 10. The aspect ratios (h/R) of the circular plate are taken to be $h/R = 0.05, 0.1, 0.15$, and 0.2.

It can be seen in Tables 1 and 2 that the current FAPM solutions are accurate and converge rapidly. The convergent solutions of L4, Q8 and C12 FAPM are obtained, when we use an $(n_r \times n_z) = (32 \times 8)$ mesh. These convergent solutions are shown to be in excellent agreement with the 3D exact solutions (Wang *et al.* 2010), quasi-3D SSDRK solutions (Wu and Liu 2016b) and 2D accurate solutions (Reddy *et al.* 1999; Saidi *et al.* 2009; Sahraee and Saidi 2009). In the cases of $h/R = 0.1$, $\kappa_{pz} = 2$, and $(n_r \times n_z) = (32 \times 8)$, the relative errors between the L4, Q8, and C12 FAPM solutions and 3D exact solutions are 0.99%, 0.25%, and 0.06%, respectively, for the clamped edges cases, while they are 0.1%, 0.1%, and 0.02% for the simply-supported edges cases. The performance of these FAPM are C12 > Q8 > L4, in which the symbol ">" means that the solutions are more accurate and that the convergence rate is faster. The convergence rates of these FAPM for the simply-supported edges cases are slightly more rapid than those for the clamped edges cases.

To have a clearer picture with regard to the displacement and stress components induced over the domain of a more general nonhomogeneous circular plate, the authors study the static problem of a two-directional, rather than a one-directional, power-law-type FG circular plate with clamped boundary conditions and under a uniformly distributed load. The Poisson's ratio ν remains a constant (i.e., $\nu = 0.288$), the ratio of E_m/E_c is taken to be 0.396, and the effective Young's modulus of the FG circular plate are given in the same form as in Eq. (28), while the volume fraction of the metal material Γ_m is defined to obey a two-directional

Table 1 Convergence studies for various RMVT-based FAPM solutions of the displacement components at the center of one-directional power-law-type FG circular plates with clamped boundary conditions and under a uniformly distributed load

κ_{pz}	Theories	$h/R = 0.05$	$h/R = 0.1$	$h/R = 0.15$	$h/R = 0.2$
2	Current L4 finite prism method (8×2)	1.4707	1.5073	1.5681	1.6529
	Current L4 finite prism method (8×4)	1.4728	1.5159	1.5860	1.6820
	Current L4 finite prism method (16×4)	1.4264	1.4687	1.5368	1.6302
	Current L4 finite prism method (32×8)	1.4104	1.4523	1.5201	1.6140
	Current Q8 finite prism method (8×2)	1.4151	1.4541	1.5192	1.6102
	Current Q8 finite prism method (8×4)	1.4178	1.4594	1.5272	1.6210
	Current Q8 finite prism method (16×4)	1.4061	1.4460	1.5121	1.6046
	Current Q8 finite prism method (32×8)	1.4024	1.4416	1.5076	1.6004
	Current C12 finite prism method (8×2)	1.3872	1.4262	1.4915	1.5832
	Current C12 finite prism method (8×4)	1.3913	1.4316	1.4979	1.5904
	Current C12 finite prism method (16×4)	1.3962	1.4351	1.5004	1.5924
	Current C12 finite prism method (32×8)	1.3986	1.4371	1.5026	1.5951
	CPT (Reddy <i>et al.</i> 1999)	1.388	1.388	1.388	1.388
	FSDT (Reddy <i>et al.</i> 1999)	1.402	1.444	1.515	1.613
	TSDT (Saidi <i>et al.</i> 2009)	1.3882	1.4426	NA	1.6032
	FOSDT (Sahraee and Saidi 2009)	1.3882	1.4426	NA	1.6033
	SSDRK (Wu and Liu 2016b)	1.405	1.447	1.513	1.603
	3D solutions (Wang <i>et al.</i> 2010)	1.400	1.438	1.500	1.586
5	Current L4 finite prism method (8×2)	1.3080	1.3402	1.3938	1.4685
	Current L4 finite prism method (8×4)	1.3094	1.3472	1.4089	1.4932
	Current L4 finite prism method (16×4)	1.2682	1.3054	1.3653	1.4476
	Current L4 finite prism method (32×8)	1.2539	1.2907	1.3503	1.4328
	Current Q8 finite prism method (8×2)	1.2585	1.2928	1.3500	1.4301
	Current Q8 finite prism method (8×4)	1.2605	1.2971	1.3568	1.4392
	Current Q8 finite prism method (16×4)	1.2501	1.2852	1.3433	1.4247
	Current Q8 finite prism method (32×8)	1.2467	1.2813	1.3393	1.4208
	Current C12 finite prism method (8×2)	1.2335	1.2677	1.3251	1.4058
	Current C12 finite prism method (8×4)	1.2369	1.2724	1.3308	1.4121
	Current C12 finite prism method (16×4)	1.2413	1.2756	1.3330	1.4139
	Current C12 finite prism method (32×8)	1.2434	1.2772	1.3348	1.4161
	TSDT (Saidi <i>et al.</i> 2009)	1.2343	1.2821	NA	1.4235
	FOSDT (Sahraee and Saidi 2009)	1.2343	1.2822	NA	1.4237

power-law variation, as follows

$$\Gamma_m(r, z) = [(1/2) - (z/h)]^{\kappa_{pz}} [1 - (r/R)]^{\kappa_{pr}} \quad (29)$$

where κ_{pr} denotes the material-property gradient index in the radial direction.

A set of dimensionless variables are given as follows

$$\bar{u}_z = [(64D_c)/(q_0R^4)]u_z(0, \theta, z) \quad (30a)$$

$$(\bar{\sigma}_r, \bar{\tau}_{rz}, \bar{\sigma}_z) = [\sigma_r(0, \theta, z), \tau_{rz}(3R/4, \theta, z), \sigma_z(0, \theta, z)]/q_0 \quad (30b)$$

Fig. 3 shows the through-thickness distribution of the dimensionless displacement component in the thickness

direction (\bar{u}_z), the so-called deflection, induced in the two-directional FG circular plate, in which $h/R = 0.1$ and $\kappa_{pz} = \kappa_{pr} = 3$. It can be seen in Fig. 3 that the through-thickness distribution of \bar{u}_z appears to be a higher-order polynomial function, rather than a constant, as conventionally assumed in the 2D advanced and refine plate theories. The maximum value of \bar{u}_z occurs in the vicinity of the mid-plane of the FG circular plate, while the minimum value is on the bottom surface, even though the deviation of these two deflection values is very minor.

Distributions of the in-plane and transverse stress components through the thickness direction are shown in Fig. 4, in which $h/R = 0.1$ and $\kappa_{pz} = \kappa_{pr} = 0.5, 1$ and 3. The results shown in Fig. 4 indicate that these stress components

Table 2 Convergence studies for various RMVT-based FAPM solutions of the displacement components at the center of one-directional power-law-type FG circular plates with simply supported boundary conditions and under a uniformly distributed load

κ_{pz}	Theories	$h/R = 0.05$	$h/R = 0.1$	$h/R = 0.15$	$h/R = 0.2$
2	Current L4 finite prism method (8×2)	5.7459	5.7808	5.8387	5.9195
	Current L4 finite prism method (8×4)	5.7460	5.7808	5.8389	5.9201
	Current L4 finite prism method (16×4)	5.7232	5.7584	5.8170	5.8987
	Current L4 finite prism method (32×8)	5.7153	5.7508	5.8099	5.8924
	Current Q8 finite prism method (8×2)	5.7440	5.7795	5.8385	5.9208
	Current Q8 finite prism method (8×4)	5.7445	5.7803	5.8397	5.9227
	Current Q8 finite prism method (16×4)	5.7234	5.7590	5.8182	5.9009
	Current Q8 finite prism method (32×8)	5.7157	5.7510	5.8100	5.8927
	Current C12 finite prism method (8×2)	5.7088	5.7444	5.8037	5.8866
	Current C12 finite prism method (8×4)	5.7100	5.7455	5.8046	5.8873
	Current C12 finite prism method (16×4)	5.7104	5.7457	5.8047	5.8873
	Current C12 finite prism method (32×8)	5.7107	5.7459	5.8048	5.8875
	CPT (Reddy <i>et al.</i> 1999)	5.700	5.700	5.700	5.700
	FSDT (Reddy <i>et al.</i> 1999)	5.714	5.756	5.826	5.925
	TSDT (Saidi <i>et al.</i> 2009)	5.7133	5.7546	5.8232	5.9194
	3D solutions (Wang <i>et al.</i> 2010)	5.710	5.745	5.804	5.886
10	Current L4 finite prism method (8×2)	4.7296	4.7575	4.8040	4.8689
	Current L4 finite prism method (8×4)	4.7297	4.7579	4.8049	4.8707
	Current L4 finite prism method (16×4)	4.7109	4.7394	4.7869	4.8532
	Current L4 finite prism method (32×8)	4.7044	4.7332	4.7809	4.8477
	Current Q8 finite prism method (8×2)	4.7281	4.7569	4.8046	4.8713
	Current Q8 finite prism method (8×4)	4.7285	4.7574	4.8054	4.8726
	Current Q8 finite prism method (16×4)	4.7111	4.7399	4.7878	4.8547
	Current Q8 finite prism method (32×8)	4.7047	4.7333	4.7811	4.8480
	Current C12 finite prism method (8×2)	4.6991	4.7279	4.7759	4.8429
	Current C12 finite prism method (8×4)	4.7001	4.7288	4.7766	4.8435
	Current C12 finite prism method (16×4)	4.7004	4.7290	4.7767	4.8435
	Current C12 finite prism method (32×8)	4.7007	4.7291	4.7768	4.8437
	CPT (Reddy <i>et al.</i> 1999)	4.692	4.692	4.692	4.692
	FSDT (Reddy <i>et al.</i> 1999)	4.704	4.739	4.799	4.882
	TSDT (Saidi <i>et al.</i> 2009)	4.7033	4.7382	4.7964	4.8778
	3D solutions (Wang <i>et al.</i> 2010)	4.698	4.726	4.774	4.840

appear to be the higher-order polynomial function variations through the thickness direction. The in-plane stress and transverse normal stress components change drastically along the thickness direction when the values of κ_{pz} and κ_{pr} become greater. In the cases of $\kappa_{pz} = \kappa_{pr} = 3$, the maximum in-plane, transverse shear, and transverse normal stress components occur at the top surface, mid-plane, and top surface of the FG circular plate, respectively, the corresponding values of which are $52.99 q_0$, $-5.64 q_0$, and q_0 , i.e., the magnitude ratios among these peak values are about 50: 5: 1 for the moderately thick plate ($h/R = 0.1$). Note that the traction conditions on the top and bottom surfaces of the FG plate are exactly satisfied, which should have been hard to achieve when using the principle of virtual displacement (PVD)-based finite element methods in

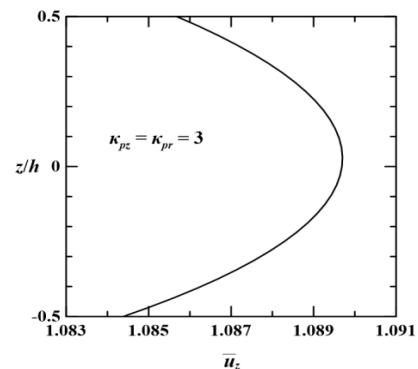


Fig. 3 The through-thickness distribution of \bar{u}_z induced in a clamped, two-directional power-law-type FG circular plate with $\kappa_{pz} = \kappa_{pr} = 3$

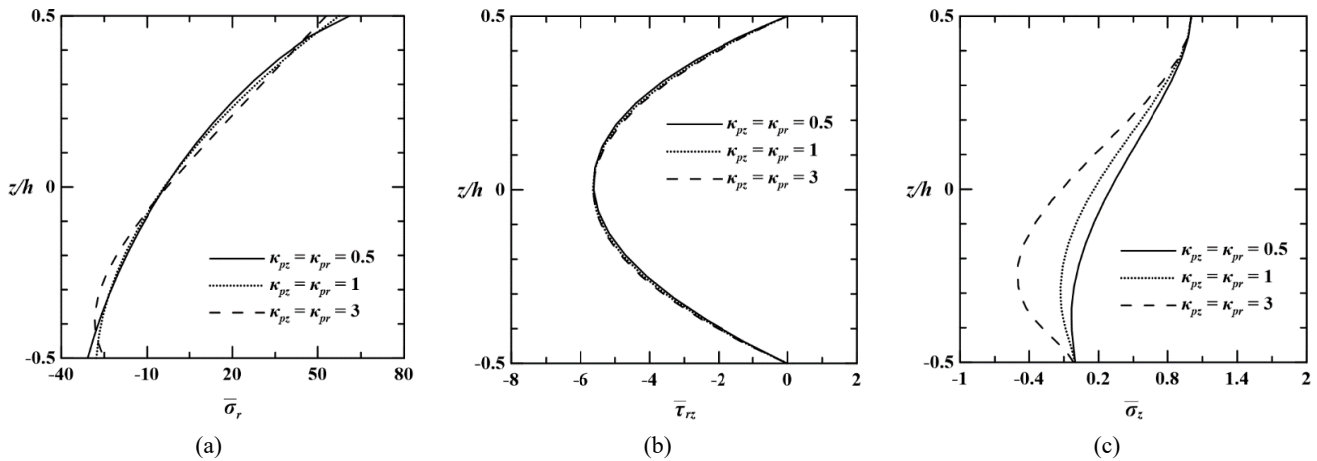


Fig. 4 Through-thickness distributions of (a) in-plane stress component, (b) transverse shear stress component, and (c) transverse normal stress component, induced in a clamped, two-directional power-law-type FG circular plate for $\kappa_{pz} = \kappa_{pr} = 0.5, 1$ and 3

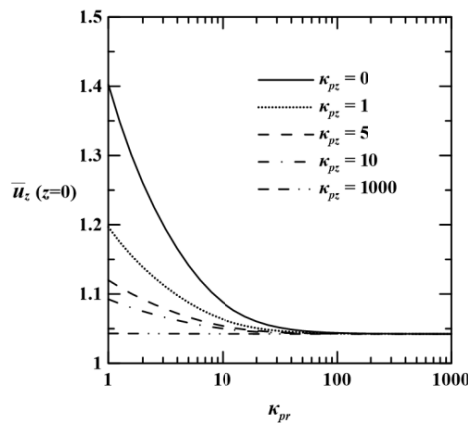


Fig. 5 Variations of \bar{u}_z at the center of a clamped, two-directional power-law-type FG circular plate with different values of κ_{pz} and κ_{pr}

most of the commercial software, such as ANSYS, ABAQUS and NASTRAN.

Fig. 5 shows the deflection induced at the center of the FG circular plate for different values of κ_{pz} and κ_{pr} , in which $h/R = 0.1$; $\kappa_{pz} = 0, 1, 5, 10$, and 1000 , and $\kappa_{pr} = 1 - 1000$. It can be seen in Fig. 5 that the deflection increase when the values of κ_{pz} and κ_{pr} become smaller, which also means the volume fraction of the metal material becomes greater, such that the gross stiffness of the FG plate becomes softer. In the cases of $\kappa_{pz} = 1$, the dimensionless central deflections of the plate decrease from 1.1967 to 1.0424 when the values of κ_{pr} change from 1 to 1000, while these decrease from 1.1967 to 1.0431 in the cases of $\kappa_{pr} = 1$ and $\kappa_{pz} = 1 - 1000$. The results show that the effects of the material-property gradient indices on the dimensionless central deflections of the plate are significant, and the degree of influence of κ_{pz} on the dimensionless central deflections of the plate is almost equivalent to that of κ_{pr} on the dimensionless central deflections of the plate when the volume fraction of the plate is defined in the form of Eq. (29).

3.2 Two-directional exponential function-type FG circular plates

In this section, the authors investigate the static behavior of a two-directional exponential function-type FG circular plate with various boundary conditions and subjected to a uniformly distributed load. The Young’s modulus of the FG circular plate is considered to obey a two-directional exponential function distribution over the radial-thickness surface, while the Poisson’s ratio of this remains a constant. They are given as follows

$$E(r, z) = E_0 e^{\kappa_{ez}[0.5+(z/h)]} e^{\kappa_{er}(r/R)} \tag{31a}$$

$$\nu = 0.3 \tag{31b}$$

where E_0 denotes the Young’s modulus at the central point of the bottom surface, $E_0 = 380$ GPa, and κ_{er} and κ_{ez} are the material-property gradient indices in the radial and thickness directions, respectively.

Table 3 shows the displacement components, $u_z(r, z = -h/2)$, of the FG circular plate obtained using the current L4, Q8 and C12 FAPM with clamped and simply-supported edges and different meshes, such as $(n_r \times n_z) = (8 \times 4), (16 \times 4), (16 \times 8)$ and (32×8) , in which $\kappa_{er} = \kappa_{ez} = 1, h = 0.1$ m, and $R = 1$ m. The current issue for the clamped edges was also studied by Nie and Zhong (2007) using the 3D state space differential quadrature (SSDQ) method and ANSYS software, the results for which are thus used to validate the performance of assorted FAPM.

It can be seen in Table 3 that the performance of these FAPM is $C12 > Q8 > L4$ when comparing their solutions with the solutions obtained using the 3D SSDQ method, in which the symbol “>” represents more accurate solutions and a faster convergence rate. The convergent FAPM solutions are obtained when a 32×8 mesh is used, which closely agree the 3D analytical solutions and accurate finite element solutions obtained using the SSDQ method and ANSYS software, respectively. The relative errors of the deflection components at $r/R = 0$ between the current L4,

Table 3 Convergence studies for various RMVT-based FAPM solutions of the displacement components at $z = -h/2$ of two-directional exponential function-type FG circular plates with simply supported and clamped boundary conditions and under a uniformly distributed load

BCs	Theories	$r/R = 0$	$r/R = 0.25$	$r/R = 0.5$	$r/R = 0.75$
Clamped	Current L4 finite prism method (8×4)	0.1587	0.1301	0.0773	0.0244
	Current L4 finite prism method (16×4)	0.1550	0.1297	0.0777	0.0248
	Current L4 finite prism method (16×8)	0.1551	0.1298	0.0778	0.0249
	Current L4 finite prism method (32×8)	0.1538	0.1301	0.0781	0.0251
	Current Q8 finite prism method (8×4)	0.1544	0.1299	0.0779	0.0249
	Current Q8 finite prism method (16×4)	0.1533	0.1301	0.0781	0.0251
	Current Q8 finite prism method (16×8)	0.1535	0.1302	0.0782	0.0252
	Current Q8 finite prism method (32×8)	0.1530	0.1303	0.0783	0.0252
	Current C12 finite prism method (8×4)	0.1521	0.1298	0.0780	0.0250
	Current C12 finite prism method (16×4)	0.1524	0.1301	0.0782	0.0252
	Current C12 finite prism method (16×8)	0.1526	0.1302	0.0783	0.0252
	Current C12 finite prism method (32×8)	0.1526	0.1303	0.0783	0.0253
	3D solutions (Nie and Zhong 2007)	0.1523	0.1297	0.0776	0.0247
	ANSYS (Nie and Zhong 2007)	0.1513	0.1289	0.0775	0.0250
Simply supported	Current L4 finite prism method (8×2)	0.6938	0.6265	0.4618	0.2393
	Current L4 finite prism method (8×4)	0.6944	0.6271	0.4622	0.2395
	Current L4 finite prism method (16×4)	0.6915	0.6266	0.4623	0.2398
	Current L4 finite prism method (16×8)	0.6915	0.6267	0.4624	0.2398
	Current Q8 finite prism method (8×2)	0.6940	0.6272	0.4627	0.2401
	Current Q8 finite prism method (8×4)	0.6941	0.6273	0.4628	0.2401
	Current Q8 finite prism method (16×4)	0.6916	0.6269	0.4627	0.2401
	Current Q8 finite prism method (16×8)	0.6916	0.6269	0.4627	0.2401
	Current C12 finite prism method (8×2)	0.6897	0.6265	0.4624	0.2399
	Current C12 finite prism method (8×4)	0.6899	0.6267	0.4626	0.2400
	Current C12 finite prism method (16×4)	0.6900	0.6268	0.4627	0.2401
	Current C12 finite prism method (16×8)	0.6901	0.6268	0.4627	0.2401

Q8, and C12 FAPM solutions and the 3D SSDQ solutions are 0.98%, 0.46%, and 0.20%, respectively. As Nie and Zhong (2007) mentioned, the finite element solutions using ANSYS are obtained using a 3D eight-node solid element code, in which the total numbers of elements and nodes are 14,549 and 16,745, respectively, while in the current FAPM analysis, these are 256 C12 prism elements with 1,401 nodes for a 32×8 mesh, 256 Q8 prism elements with 849 nodes, and 256 L4 prism elements with 297 nodes. Comparing the accuracy between the finite element solutions obtained using ANSYS software and the current FAPM as well as the numbers of nodes used, it is shown that the current FAPM are superior to the finite element codes in the commercial software ANSYS for the static analysis of two-directional FG circular plates.

A parametric study with regard to the variations of the displacement and stress components induced through the thickness direction with different values of κ_{er} and κ_{ez} and the effects of κ_{er} and κ_{ez} on the deflection of the FG circular plate with simply-supported edges is presented in Figs. 6-7 and 8, respectively, in which the dimensionless variables are defined the same as those used in Example 3.1, except that

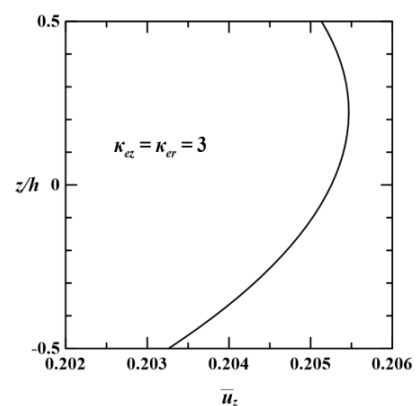


Fig. 6 The through-thickness distribution of \bar{u}_z induced in a simply-supported, two-directional exponential function-type FG circular plate with $\kappa_{pz} = \kappa_{pr} = 3$

the variable of E_c in the dimensionless displacement form is replaced with E_0 .

Fig. 6 shows the through-thickness distribution of \bar{u}_z induced in the two-directional exponential function-type FG

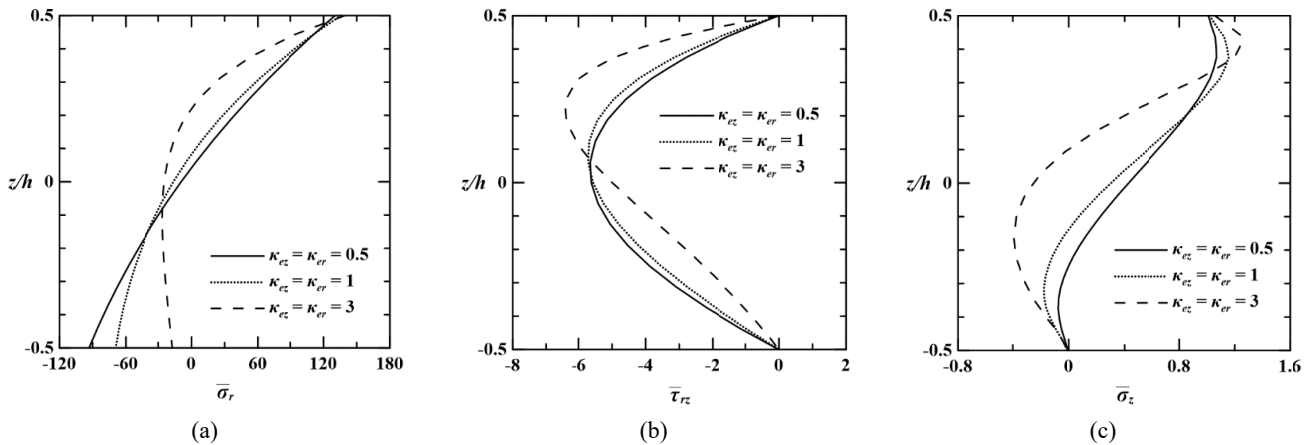


Fig. 7 Through-thickness distributions of (a) in-plane stress component; (b) transverse shear stress component; and (c) transverse normal stress component, induced in a simply-supported, two-directional exponential function-type FG circular plate for $\kappa_{pz} = \kappa_{pr} = 0.5, 1$ and 3

circular plate, in which $h/R = 0.1$ and $\kappa_{ez} = \kappa_{er} = 3$. Again, it is shown that the through-thickness distribution of \bar{u}_z appears to be a higher-order polynomial function, and its maximum value occurs in the vicinity of a quarter thickness away from the top surface of the plate, while its minimum value occurs on the bottom surface.

Fig. 7 shows distributions of the in-plane and transverse shear and normal stress components through the thickness direction, in which $h/R = 0.1$ and $\kappa_{ez} = \kappa_{er} = 0.5, 1$ and 3 . It can be seen in Fig. 7 that these stress components appear to be the higher-order polynomial function variations through the thickness direction. In the cases of $\kappa_{ez} = \kappa_{er} = 3$, the maximum in-plane, transverse shear and transverse normal stress components occur on the top surface, $z = 0.2188h$ and $z = 0.4375h$ of the FG circular plate, respectively, the corresponding values of which are $139.36 q_0$, $-6.42 q_0$, and $1.26 q_0$, i.e., the magnitude ratios among these peak values are about $110 : 5 : 1$ for the moderately thick plate ($h/R = 0.1$). As shown in Figs. 4 and 7, the through-thickness distributions of the in-plane stress and transverse stress components induced in the two-directional exponential function-type FG circular plates change more drastically than those induced in the two-directional power-law-type FG circular plates when the values of material-property gradient indices become greater. Figs. 7(b) and (c) also show that the traction conditions on the top and bottom surfaces of the FG plate are exactly satisfied.

Fig. 8 shows the deflection induced at the center of the FG circular plate for different values of κ_{ez} and κ_{er} , in which $h/R = 0.1$; $\kappa_{ez} = 0, 0.5, 1, 1.5,$ and 2 ; $\kappa_{er} = 0 - 2$. It can be seen in Fig. 8 that the deflection increase when the values of κ_{ez} and κ_{er} become smaller. In the cases of $\kappa_{ez} = 1$, the dimensionless central deflections of the plate decrease from 2.5172 to 0.9263 when the values of κ_{er} change from 0 to 2 ; while they decrease from 2.5246 to 0.955 when the values of κ_{ez} change from 0 to 2 in the cases of $\kappa_{er} = 1$. As compared with the results shown in Figs. 5 and 8, it is shown that the effects of the material-property gradient indices on the dimensionless central deflections of the two-directional exponential function-type FG circular plate are more significant than those on the dimensionless deflections

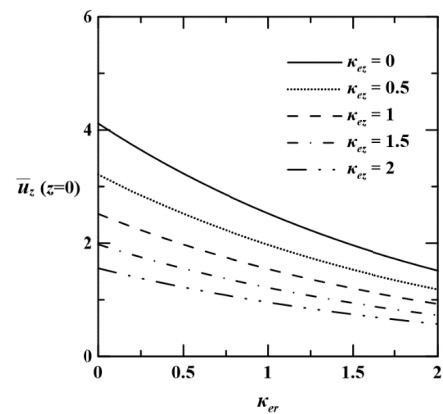


Fig. 8 Variations of \bar{u}_z at the center of a simply-supported, two-directional exponential function-type FG circular plate with different values of κ_{ez} and κ_{er}

of the two-directional power-law-type FG circular plate, which is mainly due to the fact that the degree of heterogeneity of the former is more severe than that of the latter.

4. Conclusions

In this work, the authors develop a weak-form formulation of various RMVT-based FAPM to investigate the static behavior of two-directional power-law-type and exponential function-type FG circular plates with simply-supported and clamped edges and under mechanical loads. Implementation of these FAPM shows that their convergent solutions closely agree with each other and that these solutions are in excellent agreement with the 3D exact solutions and 2D accurate solutions available in the literature. The performance of assorted FAPM is $C12 > Q8 > L4$, in which the symbol “>” represents more accurate results and a rapid convergence rate. In the numerical examples, it is also shown that the current FAPM are superior to the PVD-based finite element methods used in

the commercial software ANSYS by comparing the solutions obtained using the current FAPM and ANSYS with the 3D exact solutions available in the literature, as well as the total numbers of nodes used in the current FAPM and ANSYS software.

Some 3D static behavior of the two-directional FG circular plates under mechanical loads is captured in the numerical examples. The through-thickness distribution of the displacement component in the thickness direction appears to be a higher-order polynomial function, rather than a constant as is conventionally assumed to be the case in the 2D advanced and refined plate theories. The results also show that distributions of the in-plane and transverse stress components appear to be much higher-order polynomial functions through the thickness direction, and these variables change drastically along the thickness direction when the material-property gradient indices become greater, i.e., when the degree of heterogeneity of the FG plate becomes severe. These observations are helpful for making the kinematic and kinetic assumptions *a priori* when an advanced or refined plate theory for nonhomogeneous circular plates is to be developed.

The current FAPM can be regarded as the semi-analytical finite element methods, and these are suitable for the 3D elasticity analysis of annular and circulate plates, the corresponding coefficients of the system equations in the circumferential direction are constants, while they are variable coefficients through the thickness-meridional surface. The benefits of the current FAPM are that the quasi-3D solutions can be obtained using the computational complexity of the 2D finite element methods only and that the current FAPM can be straightforwardly extended to the analysis of assorted multilayered FG shells of revolution, such as truncated conical shells, annular spherical shells, and toroidal shells. The relevant research work is ongoing.

Acknowledgments

This work was supported by the Ministry of Science and Technology of the Republic of China through grant MOST 106-2221-E-006-036-MY3.

References

- Abdelaziz, H.H., Meziane, M.A.A., Bousahla, A.A., Tounsi, A., Mahmoud, S.R. and Alwabli, A.S. (2017), "An efficient hyperbolic shear deformation theory for bending, buckling and free vibration of FGM sandwich plates with various boundary conditions", *Steel Compos. Struct., Int. J.*, **25**(6), 693-704.
- Benchohra, M., Driz, H., Bakora, A., Tounsi, A., Bedia, E.A.A. and Mahmoud, S.R. (2018), "A new quasi-3D sinusoidal shear deformation theory for functionally graded plates", *Struct. Eng. Mech., Int. J.*, **65**(1), 19-31.
- Bouchafa, A., Bouiadjra, M.B., Houari, M.S.A. and Tounsi, A. (2015), "Thermal stresses and deflections of functionally graded sandwich plates using a new refined hyperbolic shear deformation theory", *Steel Compos. Struct., Int. J.*, **18**(6), 1493-1515.
- Bouderba, B., Houari, M.S.A., Tounsi, A. and Mahmoud, S.R. (2016), "Thermal stability of functionally graded sandwich plates using a simple shear deformation theory", *Struct. Eng. Mech., Int. J.*, **58**(3), 397-422.
- Carrera, E. and Brischetto, S. (2009), "A survey with numerical assessment of classical and refined theories for the analysis of sandwich plates", *Appl. Mech. Rev.*, **62**(1), 010803. (17 pages)
- Elmossouess, B., Kebdani, S., Bouiadjra, M.B. and Tounsi, A. (2017), "A novel and simple HSDT for thermal buckling response of functionally graded sandwich plates", *Struct. Eng. Mech., Int. J.*, **62**(4), 401-415.
- Hachemi, H., Kaci, A., Houari, M.S.A., Bourada, M., Tounsi, A. and Mahmoud, S.R. (2017), "A new simple three-unknown shear deformation theory for bending analysis of FG plates resting on elastic foundations", *Steel Compos. Struct., Int. J.*, **25**(6), 717-726.
- Houari, M.S.A., Tounsi, A., Bessaim, A. and Mahmoud, S.R. (2016), "A new simple three-unknown sinusoidal shear deformation theory for functionally graded plates", *Steel Compos. Struct., Int. J.*, **22**(2), 257-276.
- Jabbari, M., Shahryari, E., Haghghat, H. and Eslami, M.R. (2014), "An analytical solution for steady state three dimensional thermoelasticity of functionally graded circular plates due to axisymmetric loads", *Eur. J. Mech. A-Solids*, **47**, 124-142.
- Koizumi, M. (1997), "FGM activities in Japan", *Compos. Part B-Eng.*, **28**(1-2), 1-4.
- Li, X.Y., Li, P.D. and Kang, G.Z. (2012), "Axisymmetric thermoelasticity field in a functionally graded circular plate of transversely isotropic material", *Math. Mech. Solids*, **18**(5), 464-475.
- Liew, K.M., Lei, Z.X. and Zhang, L.W. (2015), "Mechanical analysis of functionally graded carbon nanotube reinforced composites: A review", *Compos. Struct.*, **120**, 90-97.
- Miyamoto, Y., Kaysser, W.A., Rabin, B.H., Kawasaki, A. and Ford, R.G. (1999), *Functionally Graded Materials: Design, Processing and Applications*, Kluwer Academic, Boston, USA.
- Nie, G. and Zhong, Z. (2007), "Axisymmetric bending of two-directional functionally graded circular and annular plates", *Acta Mech. Solida Sinica*, **20**(4), 289-295.
- Pendhari, S.S., Kant, T., Desai, Y. and Subbaiah, C.V. (2012), "Static solutions for functionally graded simply supported plates", *Int. J. Mech. Mater. Des.*, **8**(1), 51-69.
- Reddy, J.N., Wang, C.M. and Kitipornchai, S. (1999), "Axisymmetric bending of functionally graded circular and annular plates", *Eur. J. Mech. A-Solids*, **18**(2), 185-199.
- Sahraee, S. and Saidi, A.R. (2009), "Axisymmetric bending analysis of thick functionally graded circular plates using fourth-order shear deformation theory", *Eur. J. Mech. A-Solids*, **28**(5), 974-984.
- Saidi, A.R., Rasouli, A. and Sahraee, S. (2009), "Axisymmetric bending and buckling analysis of thick functionally graded circular plates using unconstrained third-order shear deformation plate theory", *Compos. Struct.*, **89**(1), 110-119.
- Sobhy, M. (2013), "Buckling and free vibration of exponentially graded sandwich plates resting on elastic foundations under various boundary conditions", *Compos. Struct.*, **99**, 76-87.
- Sobhy, M. (2015), "Thermoelastic response of FGM plates with temperature-dependent properties resting on variable elastic foundations", *Int. J. Appl. Mech.*, **7**(6), 1550082.
- Sobhy, M. (2016), "An accurate shear deformation theory for vibration and buckling of FGM sandwich plates in hygrothermal environment", *Int. J. Mech. Sci.*, **110**, 62-77.
- Tahouneh, V. (2014), "Free vibration analysis of bidirectional functionally graded annular plates resting on elastic foundations using differential quadrature method", *Struct. Eng. Mech., Int. J.*, **52**(11), 663-686.
- Tornabene, F. (2009), "Free vibration analysis of functionally graded conical, cylindrical shell and annular plate structures

- with a four-parameter power-law distribution”, *Comput. Methods Appl. Mech. Engrg.*, **198**, 2911-2935.
- Tornabene, F. and Viola, E. (2009a), “Free vibrations of four-parameter functionally graded parabolic panels and shells of revolution”, *Eur. J. Mech. A/Solids*, **28**, 991-1013.
- Tornabene, F. and Viola, E. (2009b), “Free vibration analysis of functionally graded panels and shells of revolution”, *Meccanica*, **44**, 255-281.
- Tornabene, F., Fantuzzi, N. and Bacciocchi, M. (2017a), “Strong and weak formulations based on differential and integral quadrature methods for the free vibration analysis of composite plates and shells: Convergence and accuracy”, *Eng. Ana. Bound. Elem.* DOI: doi.org/10.1016/j. engana-bound.2017
- Tornabene, F., Fantuzzi, N. and Bacciocchi, M. (2017b), “A new doubly-curved shell element for the free vibrations of arbitrarily shaped laminated structures based on weak formulation isogeometric analysis”, *Compos. Struct.*, **171**, 429-461.
- Wang, Y., Xu, R.Q. and Ding, H.J. (2009), “Free axisymmetric vibration of FGM circular plates”, *Appl. Math. Mech.*, **30**(9), 1077-1082.
- Wang, Y., Xu, R.Q. and Ding, H.J. (2010), “Three-dimensional solution of axisymmetric bending of functionally graded circular plates”, *Compos. Struct.*, **92**(7), 1683-1693.
- Wu, C.P. and Li, H.Y. (2013a), “An RMVT-based finite rectangular prism method for the 3D analysis of sandwich FGM plates with various boundary conditions”, *CMC-Comput. Mater. Continua*, **34**(1), 27-62.
- Wu, C.P. and Li, H.Y. (2013b), “RMVT-based finite cylindrical prism methods for multilayered functionally graded circular hollow cylinders with various boundary conditions”, *Compos. Struct.*, **100**, 592-608.
- Wu, C.P. and Liu, Y.C. (2016a), “A review of semi-analytical numerical methods for laminated composite and multilayered functionally graded elastic/piezoelectric plates and shells”, *Compos. Struct.*, **147**, 1-15.
- Wu, C.P. and Liu, Y.C. (2016b), “A state space meshless method for the 3D analysis of FGM axisymmetric circular plates”, *Steel Compos. Struct.*, **22**(1), 161-182.
- Xu, R.Q., Wang, Y. and Chen, W.Q. (2005), “Axisymmetric buckling of transversely isotropic circular and annular plates”, *Arch. Appl. Mech.*, **74**(10), 692-703.